Andreev reflection in two-dimensional relativistic materials with realistic tunneling transparency in normal-metal/superconductor junctions

Yung-Yeh Chang,[1,*] Chung-Yu Mou,[2,3,4,†] and Chung-Hou Chung[1,3,4,‡]

[1]*Department of Electrophysics, National Chiao Tung University, Hsinchu 30010, Taiwan, Republic of China*

[2]*Department of Physics, National Tsing Hua University, Hsinchu 30043, Taiwan, Republic of China*

[3]*Institute of Physics, Academia Sinica, Nankang 11529, Taiwan, Republic of China*

[4]*Physics Division, National Center for Theoretical Sciences, P. O. Box 2-131, Hsinchu 30043, Taiwan, Republic of China*

(Received 20 February 2017; published 17 August 2017)

The Andreev conductance across realistic two-dimensional (2D) normal-metal (N)/superconductor (SC) junctions with a relativistic Dirac spectrum is theoretically investigated within the Blonder-Tinkham-Klapwijk formalism with tunable tunneling transparency. It is known that due to the effect of Klein tunneling, impurity potentials at the interface of 2D relativistic materials will enhance (not suppress) the tunneling and therefore are not suitable to model a realistic tunnel junction of these materials. Here, we propose a way to construct a more realistic tunnel junction by adding a narrow, homogeneous local strain, which effectively generates a δ-gauge potential and variations of electron hopping at the interface, to adjust the transparency of the N/SC junction. Remarkable suppression of the Andreev conductance is indeed observed in the graphene N/SC junction as the strength of the local strain increases. We also explore the Andreev conductance in a topological N/SC junction at the two inequivalent Dirac points and predict the distinctive behaviors for the conductance across the chiral-to-helical topological phase transition. The relevance of our results for the adatom-doped graphene is discussed.

DOI: 10.1103/PhysRevB.96.054514

I. INTRODUCTION

The Andreev reflection (AR) is a scattering process associated with the electron-hole conversion which occurs between a normal metal (N) and a superconductor (SC) with the excitation energy of the incident electrons being lower than the superconducting gap energy [1].

Microscopically, an incident electron, upon hitting the N/SC interface, is reflected back as a hole which follows the same trajectory as the incident electron but carries opposite spin, thus being called the retro Andreev reflection (RAR). RAR has been extensively studied in conventional s-wave superconductors within the Blonder-Tinkham-Klapwijk (BTK) formalism [2]. In 2006, Beenakker unveiled a different type of AR process for relativistic electrons in a graphene-based N/SC junction, known as the specular Andreev reflection (SAR) since the hole reflection, in this case, resembles the mirrorlike reflection of light [3,4], and a transition between retro-to-specular AR was also predicted.

SAR was also theoretically proposed to occur in a two-dimensional (2D) semiconductor-superconductor junction with finite Rashba spin-orbit (SO) coupling [5]. To date, AR has been studied extensively in a variety of 2D N/SC junctions with underlying honeycomb-lattice structure and different types of pairing symmetries [6–10].

More interestingly, it has been pointed out that the zero-bias peak of the Andreev conductance spectroscopy could serve as an experimental signature to identify the existence of Majorana bound states [11,12]. Until recently, the SAR and the specular-to-retro AR transition were experimentally confirmed on graphene-based superconducting junctions [13,14]. It is therefore of great importance to investigate AR in the N/SC junction on a honeycomb lattice.

Despite extensive studies on AR for 2D N/SC junctions with a relativistic Dirac spectrum, theoretical approaches to date based on BTK formalism are all under the (somewhat unrealistic) assumption of the transparency of the junction. It is therefore difficult to account for the recent experiments where suppression of tunneling conductance has clearly been observed due to a finite barrier at the interface [14].

It is also known that for relativistic materials due to the "Klein tunneling" effect the impurity potentials tend to enhance rather than suppress the tunneling current [15]. In this paper, we propose a possible way to construct a more realistic N/SC junction with tunable tunneling transparency.

Unlike the conventional BTK formalism [2] in which the transparency of the tunnel junction is simulated by the impurity potential across the junction, here, we provide an alternative approach to control the transparency of a N/SC junction on a honeycomb lattice by applying a homogeneous, narrow local strain parallel to the interface of junctions. Our approach generalizes the idea shown in Refs. [16,17] that adding narrow strain effectively generates a δ-gauge potential at the N/SC interface, which introduces variations of the electron hopping at the interface and therefore changes the tunneling transparency. To examine the effect of this tunable δ potential, we first compute Andreev conductance of the graphene normal-metal/$(d + id')$-wave superconductor junction in the presence of a δ-gauge potential via BTK formalism [2]. Unlike the enhancement of tunneling current due to the Klein tunneling in graphene, a remarkable suppression of the Andreev conductance is indeed observed with increasing the strength of the local strain. The conductance suppression in this case is analogous to the effect of a potential barrier at the interface of a conventional one-dimensional (1D) N/s-wave-SC junction in the BTK

*cdshjtr@gmail.com

†mou@phys.nthu.edu.tw

‡chung@mail.nctu.edu.tw

framework [2] despite a different mechanism. Next, we apply our theory to a 2D topological N/SC junction. Due to the broken valley degeneracy [18,19], the Andreev conductance from the incident electrons near the two Dirac points exhibits entirely different behaviors. We make predictions by providing profiles of the Andreev conductance within certain parameter regimes for future experiments. The remaining parts of this paper are organized as follows: In Sec. II, we apply our approach to compute AR across a graphene-$(d+id')$-wave N/SC junction in the presence of a δ-gauge field. In Sec. III, we further compute AR in a different system made of the Kane-Mele/$(d+id')$-wave N/SC junction on a honeycomb lattice. In Sec. IV, we provide a discussion and conclusions.

II. AR ACROSS A GRAPHENE-$(d+id')$-WAVE N/SC JUNCTION IN THE PRESENCE OF A δ-GAUGE FIELD

In this section, we start by briefly reviewing the electron motions in a graphene monolayer within the tight-binding formalism in Sec. II A. The configuration of the lattice structure for a single-layer graphene sheet is schematically illustrated in the unshaded region of Fig. 1(a). The derivations of the effective δ-gauge potential via adding a narrow, homogeneous local strain on graphene will be given in Sec. II B. Finally, we apply the BTK formalism [2] to compute the Andreev conductance across a graphene normal-metal/$(d+id')$-wave N/SC junction to examine the effect of the δ-gauge potential. The results are provided in Sec. II C.

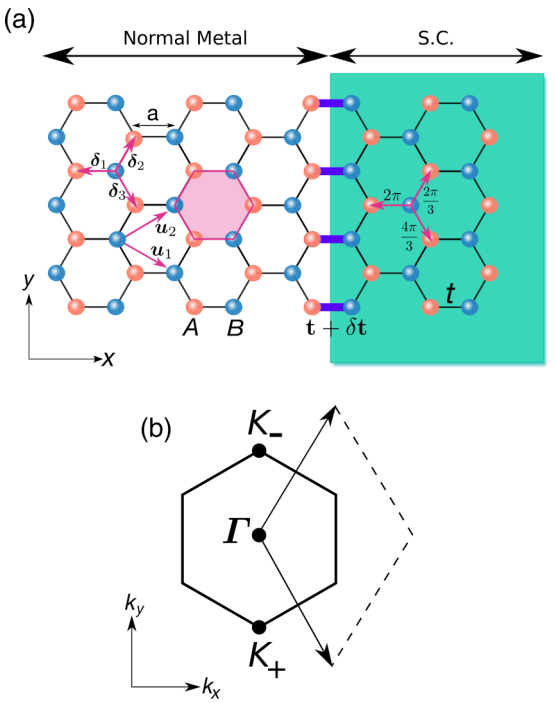

FIG. 1. We consider a N/SC junction which is composed of a normal metal (N) occupying the left side connected to the superconducting (SC) region on the right (green shaded area) with underlying honeycomb lattice structure as depicted in (a). The unit length is chosen to be the nearest-neighbor lattice spacing $a=1$ throughout this paper. The three phases for the bond-dependent $d+id'$ pairing are defined as $\varphi_{a=1,2,3}=2(a-1)\pi/3$, as shown in the SC region in (a). The thicker purple horizontal bonds which locate at the N/SC interface represent the modified hopping strength $t+\delta t$ due to the local strain. The first Brillouin zone is shown in (b).

A. Electronic properties in a graphene monolayer

The electronic motion in a uniform undoped graphene monolayer is often formulated by the nearest-neighbor tight-binding model [17,20]:

$$H_0 = -t\sum_{\langle i,j\rangle}(c^\dagger_{A,i}c_{B,j}+\text{H.c.}) = \sum_{\boldsymbol{k}\in BZ}(f(\boldsymbol{k})c^\dagger_{A,\boldsymbol{k}}c_{B,\boldsymbol{k}}+\text{H.c.}), \quad (1)$$

where $c_{\alpha,i}$ ($c^\dagger_{\alpha,i}$) annihilates (creates) an electron on the $\alpha\in\{A,B\}$ sublattice in the ith unit cell. The electron operators in momentum space are given by the Fourier transform of $c_{\alpha,i}$: $c_{\alpha,\boldsymbol{k}}=(1/\sqrt{N_s})\sum_i e^{i\boldsymbol{k}\cdot\boldsymbol{R}_i}c_{\alpha,i}$, with $\boldsymbol{R}_i$ being the position vector of the ith unit cell and N_s being the total number of unit cells. Nearest-neighbor lattice vectors are $\boldsymbol{\delta}_{1,2,3}$ with unit length a, as shown in Fig. 1(a). Here, we set $a=1$ in what follows. The constant prefactor t represents the hopping strength between two nearest-neighbor electrons. $f(\boldsymbol{k})\equiv -t\sum_{i=1}^3 e^{i\boldsymbol{k}\cdot\boldsymbol{\delta}_i}$ is a $\boldsymbol{k}$-dependent function which characterizes the band structures. The undoped single-layer graphene based on the tight-binding Hamiltonian in Eq. (1) features the well-known Dirac band structure with linear spectrum on the Dirac points, as shown in Fig. 1(b):

$$\boldsymbol{K}_+=\left(0,-\frac{4\pi}{3\sqrt{3}}\right),\quad \boldsymbol{K}_-=\left(0,\frac{4\pi}{3\sqrt{3}}\right). \quad (2)$$

The linear dispersion is governed by the linearized Hamiltonian around the Dirac points, which is given by $H=H_+ + H_- = \sum_{\boldsymbol{q},\tau=\pm}\Psi^\dagger_\tau(\boldsymbol{q})\mathcal{H}_\tau(\boldsymbol{q})\Psi_\tau(\boldsymbol{q})$ subject to the condition $|\boldsymbol{q}|\ll 1$. In the momentum space, the 2×2 Dirac Hamiltonians around the Dirac points take the form of

$$\mathcal{H}_+(\boldsymbol{q})=\frac{3t}{2}\begin{pmatrix}0 & iq_x-q_y\\ -iq_x-q_y & 0\end{pmatrix} = \hbar v_F(\pi^{y*}q_x-\pi^x q_y) \quad (3)$$

and

$$\mathcal{H}_-(\boldsymbol{q})=\frac{3t}{2}\begin{pmatrix}0 & iq_x+q_y\\ -iq_x+q_y & 0\end{pmatrix} = -\hbar v_F(\pi^y q_x-\pi^x q_y), \quad (4)$$

which acts on a two-dimensional spinor $\Psi_\tau(\boldsymbol{q})=(c_{A\tau}(\boldsymbol{q}),c_{B\tau}(\boldsymbol{q}))^T$. The valley indices $\tau=\pm$ refer to the electronic states $\Psi_\tau(\boldsymbol{q})$ near $\boldsymbol{K}_\pm$. $v_F\equiv 3t/2\hbar$ is defined as the Fermi velocity for the tight-binding model of graphene. Here, $\pi^{x,y,z}$ denote the Pauli matrices:

$$\pi^x=\begin{pmatrix}0&1\\1&0\end{pmatrix},\ \pi^y=\begin{pmatrix}0&-i\\i&0\end{pmatrix},\ \pi^z=\begin{pmatrix}1&0\\0&-1\end{pmatrix}, \quad (5)$$

which are used to label the sublattices. We also defined a 2×2 unit matrix,

$$\pi^0=\begin{pmatrix}1&0\\0&1\end{pmatrix}, \quad (6)$$

for later use, which is also for the sublattices.

B. The effective δ-gauge field

One possible way to introduce disorders in graphene is to change the bond spacing between two different sites via applying a local strain, which effectively varies the hopping strength t as in Eq. (1) [16,17]. To account for the effect of the local strain, we may change the hopping strength as $t \to t + \delta t(\boldsymbol{R}_i, \boldsymbol{\delta}_a)$ in the tight-binding Hamiltonian in Eq. (1). The magnitude of $\delta t(\boldsymbol{R}_i, \boldsymbol{\delta}_a)$ can be, in general, bond dependent and spatially inhomogeneous over one bond spacing. For simplicity, $\delta t(\boldsymbol{R}_i, \boldsymbol{\delta}_a)$ here is assumed to be uniform over the bond spacing; thus, it will not acquire Fourier components in the Fourier transformation. Under these assumptions, the linearized Hamiltonian for the change in the hopping strength around the $\boldsymbol{K}_+$ valley takes the form

$$\begin{aligned}\delta H_+ &= -\int d\boldsymbol{r}[A(\boldsymbol{r})c^\dagger_{A+}(\boldsymbol{r})c_{B+}(\boldsymbol{r}) + A^*(\mathbf{r})c^\dagger_{B+}(\boldsymbol{r})c_{A+}(\boldsymbol{r})] \\ &= -\int d\boldsymbol{r}\,\Psi^\dagger_+(\boldsymbol{r})\begin{pmatrix} 0 & i\mathcal{A}_x - \mathcal{A}_y \\ -i\mathcal{A}_x - \mathcal{A}_y & 0\end{pmatrix}\Psi_+(\boldsymbol{r}) \\ &= -\int d\boldsymbol{r}\,\Psi^\dagger_+(\boldsymbol{r})(\pi^{y*}\mathcal{A}_x - \pi^x\mathcal{A}_y)\,\Psi_+(\boldsymbol{r}), \end{aligned} \tag{7}$$

where $\Psi_\tau(\boldsymbol{r}) = (c_{A\tau}(\boldsymbol{r}), c_{B\tau}(\boldsymbol{r}))^T$ denotes the field operator for the $\boldsymbol{K}_\tau$ valley, while

$$A(\boldsymbol{r}) \equiv \sum_{a=1}^{3} \delta t(\boldsymbol{r},\boldsymbol{\delta}_a)e^{i\boldsymbol{K}\cdot\boldsymbol{\delta}_a} \equiv i\mathcal{A}_x(\boldsymbol{r}) - \mathcal{A}_y(\boldsymbol{r}) \tag{8}$$

is a complex function. Here, $\mathcal{A}_x$ and A_y are real functions. If we assume that the effect of the local strain extends over only one lattice spacing and influences only the horizontal bonds along the y direction, as shown in Fig. 1(a), the complex function $A(\boldsymbol{r})$ in Eq. (8) can be reduced to the form of a δ function. In units of $\hbar = v_F = 1$, $A(\boldsymbol{r})$ simply takes the form

$$A(\boldsymbol{r}) = \delta t(\boldsymbol{r}) = \frac{\delta t}{t}\delta(x). \tag{9}$$

Consequently, only the real part of $A(\boldsymbol{r})$ survives; the imaginary part vanishes: $\mathcal{A}_x = 0$, $\mathcal{A}_y = -\frac{\delta t}{t}\delta(x)$

The linearized Hamiltonian for the change in the hopping amplitude near the $\boldsymbol{K}_-$ valley is related to the one for the $\boldsymbol{K}_+$ valley by time-reversal transformation $\mathcal{T}$, i.e., $\delta H_- = \mathcal{T}\,\delta H_+ \mathcal{T}^{-1}$:

$$\delta H_- = -\int d^2r\,\Psi^\dagger_-(\mathbf{r})(\pi^y\mathcal{A}_x - \pi^x\mathcal{A}_y)\,\Psi_-(\mathbf{r}). \tag{10}$$

Combining Eqs. (3), (4), (7), and (10), the linearized Hamiltonian in the presence of a homogeneous local strain in real space is given by

$$H = \int d^2r\,\Psi^\dagger(\boldsymbol{r})\begin{pmatrix}\pi^{y*}(\hat{q}_x - \mathcal{A}_x) - \pi^x(\hat{q}_y - \mathcal{A}_y) & 0 \\ 0 & -[\pi^y(\hat{q}_x + \mathcal{A}_x) - \pi^x(\hat{q}_y + \mathcal{A}_y)]\end{pmatrix}\Psi(\boldsymbol{r}), \tag{11}$$

where $\Psi(\boldsymbol{r}) \equiv (\Psi_+(\boldsymbol{r}), \Psi_-(\boldsymbol{r}))^T$ and the momentum operator $\hat{q}_i \equiv -i\partial_i$. The reverse in the sign in the terms containing the complex vector $\vec{\mathcal{A}} = (\mathcal{A}_x, \mathcal{A}_y)$ for different valleys in Eq. (11) implies that $\vec{\mathcal{A}}$ can be viewed as a gauge field [16,17]. Combining Eqs. (8), (9), and Eq. (11), it is clear that the effect of a homogeneous local strain in the distance over one horizontal bond on graphene can be simply regarded as an effective δ-gauge field of a series of localized impurities along the y direction, which couples the electrons from sublattices A and B.

C. Andreev conductance across a graphene ($d_{x^2-y^2} + id'_{xy}$)-wave N/SC junction

In this section, we dedicate our efforts to investigating the Andreev reflection through a graphene normal-metal/$(d + id')$-wave spin-singlet superconductor N/SC junction with an effective δ-gauge field lying on the N/SC interface via BTK formalism.

Unlike the well-known case of superconductivity in graphene via proximity to a superconducting electrode [21], the $(d + id')$-wave spin-singlet superconducting order is induced in graphene at finite doping by on-site electron-electron Coulomb repulsion [22–24]. Due to the C_6 point-group symmetry of the underlying honeycomb lattice, the $(d + id')$-wave superconducting order in the $\boldsymbol{k}$ space takes the form

$$\Delta_{\boldsymbol{k}} = \sum_{a=1}^{3} \Delta_{\boldsymbol{\delta}_a} e^{i\boldsymbol{k}\cdot\boldsymbol{\delta}_a}, \tag{12}$$

with the bond-dependent order parameter $\Delta_{\boldsymbol{\delta}_a} = \Delta_0 e^{i\varphi_a}$, with $\varphi_a = 2(a-1)\pi/3$ [22–24].

As depicted in Fig. 1(a), the N/SC junction being considered is composed of a sheet of graphene normal metal that occupies the region of $-\infty < x < 0$ connected to a 2D superconducting thin film which occupies $0 < x < \infty$ with a sharp N/SC interface in between (i.e., at the position of $x = 0$), which implies that the translational invariance along the x direction is broken. We assume that the N/SC junction is homogeneous and infinitely extended in the y direction; therefore, the translational symmetry is preserved in y. The sharp N/SC junction signifies that the bulk value of the superconducting pairing amplitude denoted as Δ_0 is reached at a negligibly small distance from the interface, which can be achieved via adjusting the doping or gate voltage in the SC region [3,4,7].

Due to the valley and spin degeneracy, the electronic motions can be described by two sets of decoupled Dirac–Bogoliubov–de Gennes (DBdG) equations [25,26] for the $\boldsymbol{K}_+$ and $\boldsymbol{K}_-$ valleys, each containing four equations. Thus, it suffices to consider only the set for the K_- valley:

$$\begin{pmatrix}\mathcal{H}_-(\boldsymbol{q}) - \mu & \Theta(x)\Delta_-(\boldsymbol{q}) \\ \Theta(x)\Delta_-(\boldsymbol{q})^\dagger & \mu - \mathcal{H}_-(\boldsymbol{q})\end{pmatrix}\begin{pmatrix}u \\ v\end{pmatrix} = \frac{\epsilon_{\boldsymbol{q}}}{t}\begin{pmatrix}u \\ v\end{pmatrix}, \tag{13}$$

where

$$H_{-}(\boldsymbol{q}) = -(\pi^{x} q_{y} - \pi^{y} q_{x}) - (U_0/t)\pi^{0}\Theta(x) \tag{14}$$

is the 2×2 linearized single-particle Hamiltonian of graphene at the $\boldsymbol{K}_{-}$ valley and μ denotes the chemical potential. Here, $u = (u_{A\uparrow}, u_{B\uparrow})$ and $v = (v_{A\downarrow}, v_{B\downarrow})$ are the two-component $\boldsymbol{q}$-dependent wave functions for the electron (electronlike) and hole (holelike) excitations at the excitation energy $\epsilon_{\boldsymbol{q}} > 0$, which is measured relative to the chemical potential μ. Here, we introduce a unit-step electrostatic potential

$$U_0\Theta(x) = \begin{cases} U_0, & x \geqslant 0, \\ 0, & x < 0, \end{cases} \tag{15}$$

to the SC region, where U_0 can be tuned independently through doping or the gate voltage. To justify the assumption of a sharp N/SC junction as mentioned previously, the energy scales must satisfy $U_0 \gg t \gg \mu, \Delta_0$, such that the Fermi wavelength $\lambda'_F = 2\pi\hbar v_F/(\mu + U_0)$ in SC is much shorter than that in N, where $\lambda_F = 2\pi\hbar v_F/\mu$ [3,4,7]. The linearized superconducting pairing matrix $\Delta_{-}(\boldsymbol{q})$ with $d_{x^2-y^2} + id'_{xy}$ pairing symmetry at the $\boldsymbol{K}_{-}$ valley is given by

$$\Delta_{-}(\boldsymbol{q}) = \frac{\Delta_0}{t}\begin{pmatrix} 0 & -\frac{3}{2}(iq_x - q_y) \\ 3 & 0 \end{pmatrix}, \tag{16}$$

which is related to the one for the K_{+} valley by $\Delta_{+}(\boldsymbol{q}) = \Delta_{-}^{T}(-\boldsymbol{q})$. Apparently, the $(d_{x^2-y^2} + id_{xy})$-wave superconducting pairing at low energy features the s- and $(p_x + ip_y)$-pairing symmetry [6,27].

To study the Andreev reflection across a N/SC junction, we may imagine that an incident electron comes from $x = -\infty$ toward the N/SC junction and scatters by the potential at the interface. While scattering with the potential, electrons may reflect back to the N region as either normal electrons or holes or may tunnel through the barrier into the SC region as Dirac-Bogoliubov quasiparticles. For convenience, electrons are assumed to go through elastic scattering processes at the interface. Hence, the whole scattering basis for the incident, reflected, and transmitted states inside the N and SC region, which can be solved via Eq. (13), are characterized by the same excitation energy ϵ.

The real-space eigenfunctions of Eq. (13) in general take the form of plane-wave solutions, i.e.,

$$\Psi(\boldsymbol{r}) = e^{iq_x x + iq_y y}\begin{pmatrix} u_{A\uparrow} \\ u_{B\uparrow} \\ v_{A\downarrow} \\ v_{B\downarrow} \end{pmatrix}. \tag{17}$$

Note that the solutions of Eq. (13) in the SC region may be either an evanescent mode which decays exponentially with the increase in distance from the interface at an energy ϵ of the incident electron smaller than the superconducting gap, namely, $\epsilon < \Delta_{\text{gap}}$, or a propagating mode at $\epsilon > \Delta_{\text{gap}}$. Furthermore, since the Hamiltonian in the normal metal is diagonal in the spin subspace, here, we consider only the incident electrons to be spin up in Eq. (17).

Here, we denote $\psi(\boldsymbol{q}) \equiv (u, v) = (u_{A\uparrow}, u_{B\uparrow}, v_{A\downarrow}, v_{B\downarrow})$. Therefore, the total wave function $\Psi_N\,(\Psi_{sc})$ in the N (SC) region can be expressed as a superposition of various eigenstates of Eq. (13) with positive excitation energy in the region $x < 0$ ($x > 0$):

$$\begin{aligned} \Psi_N(\boldsymbol{r}) &= \psi_N^{(e)}(q_x, q_y)e^{iq_x x + iq_y y} + r_e\psi_N^{(e)}(-q_x, q_y)e^{-iq_x x + iq_y y} \\ &\quad + r_h\psi_N^{(h)}(q'_x, q_y)e^{iq'_x x + iq_y y}, \\ \Psi_{sc}(\boldsymbol{r}) &= t_e\psi_{sc}^{(e)}(\bar{q}_x, q_y)e^{i\bar{q}_x x + iq_y y} + t_h\psi_{sc}^{(h)}(-\bar{q}'_x, q_y)e^{-i\bar{q}'_x x + iq_y y}, \end{aligned} \tag{18}$$

with the incident state being normalized to unity. $r_{e,h}$ and $t_{e,h}$, which depend on the energy ϵ and the wave vector $\boldsymbol{q}$ of the incident state, represent the reflection and transmission coefficients for the electron branch (with subscript e) and hole branch (with subscript h). Due to the assumption of elastic scattering, $\psi_{N,sc}^{(e),(h)}$ are the eigenstates of Eq. (13) with the same excitation energy ϵ. Note that the transverse component of the wave vector q_y is a conserved quantity during the scattering process due to the translational symmetry in y, while the longitudinal components for the electron and hole (electronlike and holelike) states q_x, q'_x $(\bar{q}_x, \bar{q}'_x)$ can be determined via their (quasiparticle) dispersion relations at a given ϵ and q_y.

Due to the presence of a δ-gauge field as well as the restriction that the DBdG equations are first order, the wave-function continuity at the interface as widely used in various studies under the assumption of ideal N/SC interfaces is not an appropriate boundary condition. Detailed derivations for the boundary condition for our theory are provided in the following: the DBdG equations for the $\boldsymbol{K}_{-}$ valley in the presence of an effective δ-gauge field as shown in Eq. (9) are given by

$$\begin{pmatrix} 0 & i\hat{q}_x + \hat{q}_y - \frac{\delta t}{t}\delta(x) - \frac{\mu}{t} & 0 & -\frac{3\Delta_0}{2t}(i\hat{q}_x - \hat{q}_y) \\ -i\hat{q}_x + \hat{q}_y - \frac{\delta t}{t}\delta(x) - \frac{\mu}{t} & 0 & \frac{3\Delta_0}{t} & 0 \\ 0 & \frac{3\Delta_0}{t} & 0 & \frac{\mu}{t} - i\hat{q}_x - \hat{q}_y + \frac{\delta t}{t}\delta(x) \\ \frac{3\Delta_0}{2t}(i\hat{q}_x + \hat{q}_y) & 0 & \frac{\mu}{t} + i\hat{q}_x - \hat{q}_y + \frac{\delta t}{t}\delta(x) & 0 \end{pmatrix}\begin{pmatrix} f_{A\uparrow} \\ f_{B\uparrow} \\ g_{A\downarrow} \\ g_{B\downarrow} \end{pmatrix} = \frac{\epsilon}{t}\begin{pmatrix} f_{A\uparrow} \\ f_{B\uparrow} \\ g_{A\downarrow} \\ g_{B\downarrow} \end{pmatrix}. \tag{19}$$

Taking the momentum operator $\hat{q}_i \to -i\partial_i$ and integrating along the x direction over a small distance across the interface, Eq. (19) become

$$\begin{aligned}
&\left[f^{sc}_{B\uparrow}(0) - f^{N}_{B\uparrow}(0)\right] - \frac{3\Delta_0}{2t}\left[g^{sc}_{B\downarrow}(0) - g^{N}_{B\downarrow}(0)\right] = \frac{\delta t}{t} f_{B\uparrow}(0),\\
&\left[f^{N}_{A\uparrow}(0) - f^{sc}_{A\uparrow}(0)\right] = \frac{\delta t}{t} f_{A\uparrow}(0).\\
&\left[g^{sc}_{B\downarrow}(0) - g^{N}_{B\downarrow}(0)\right] = \frac{\delta t}{t} g_{B\downarrow}(0),\\
&\left[g^{N}_{A\downarrow}(0) - g^{sc}_{A\downarrow}(0)\right] + \frac{3\Delta_0}{2t}\left[f^{N}_{A\uparrow}(0) - f^{sc}_{A\uparrow}(0)\right] = \frac{\delta t}{t} g_{A\downarrow}(0).
\end{aligned} \tag{20}$$

In Eq. (B2), $f(g)_{\alpha\sigma}(0^+) \equiv f(g)^{sc}_{\alpha\sigma}$ and $f(g)_{\alpha\sigma}(0^-) \equiv f(g)^{N}_{\alpha\sigma}$, where α denotes the A or B sublattice and σ denotes the spin $\sigma = \uparrow, \downarrow$. As we shall see in Eq. (B2), the boundary condition results in an ambiguity of Ψ at $x = 0$ which results from the situation where the DBdG equations are first order. We further impose the following conditions to resolve the wave-function ambiguity: in the situation of $\Delta_0 = 0$ and $\delta t = -t$ [16], we expect no tunneling current across the N/SC junction. The conditions are quite straightforward: in the case mentioned above, the original N/SC junction reduces to two disconnected semiplanes of the graphene sheet; thus, electron tunneling is forbidden, giving rise to no tunneling current. The issue of wave-function ambiguity at the origin now changes to the problem of electron tunneling across a junction of two pure graphene semiplanes with a δ-gauge field taking the form of Eq. (9) in between. Based on the condition of current conservation and the requirement of no tunneling current across the junction at $t = -\delta t$ and $\Delta_0 = 0$, we choose the wave functions at the origin as

$$\begin{aligned}
&f_{A\sigma}(0) = f^{sc}_{A\sigma},\ f_{B\sigma}(0) = f^{N}_{B\sigma},\\
&g_{A\sigma}(0) = g^{sc}_{A\sigma},\ g_{B\sigma}(0) = g^{N}_{B\sigma},
\end{aligned} \tag{21}$$

where $\sigma = \uparrow, \downarrow$ denotes spin. Note that due to the relation of the time-reversal partner between the incident electrons and the reflected holes within the DBdG formalism [3,28] for AR in a single-layer graphene, the hole wave functions g share the same boundary conditions as the electrons wave functions f, as shown in Eq. (21), leading to

$$\begin{aligned}
f^{sc}_{B\uparrow}(0) &= \eta f^{N}_{B\uparrow}(0) + \frac{3\Delta_0}{2t}\left[g^{sc}_{B\downarrow}(0) - g^{N}_{B\downarrow}(0)\right],\\
f^{sc}_{B\downarrow}(0) &= \eta f^{sc}_{A\uparrow}(0),\\
g^{sc}_{B\downarrow}(0) &= \eta g^{N}_{B\downarrow}(0),\\
g^{N}_{A\downarrow}(0) &= \eta g^{sc}_{A\downarrow}(0) + \frac{3\Delta_0}{2t}\left[f^{sc}_{A\uparrow}(0) - f^{N}_{A\uparrow}(0)\right],
\end{aligned} \tag{22}$$

where $\eta \equiv 1 + \delta t/t$. For detailed derivations of the boundary conditions in Eq. (21), we refer readers to Appendix A. Once the reflection and transmission coefficients are obtained, following the BTK formalism [2], the normalized differential conductance can be computed by summing over all possible incident states, leading to

$$\frac{G}{G_0} = \int_0^{\pi/2} d\theta \cos\theta [1 - |r_e(eV,\theta)|^2 + |r_h(eV,\theta)|^2], \tag{23}$$

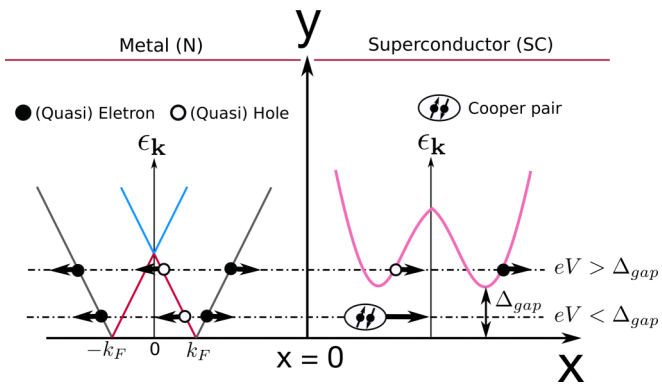

FIG. 2. Schematic plot of the band structure in the N and SC regions at the N/SC interface. In the N region, the black solid line indicates the band structure for particles, while the red and blue solid lines show the conduction- and valence-band holes. The Dirac-Bogoliubov quasiparticle dispersion is shown in the SC region The direction of the arrows represents the direction of group velocity. This figure describes a general electron-hole conversion process at different biases eV.

where G_0 is the ballistic conductance of graphene [3,6].

In the absence of the local strain $\delta t = 0$, the Andreev conductance for the graphene $(d + id')$-wave superconductor N/SC junction is reproduced [6], as shown in Figs. 3 and 4, and the specular-AR to retro-AR transition marked by $eV/t = \mu$ can be easily identified for the case of $\Delta_{\text{gap}} > \mu$. The behaviors of the normalized differential conductance G/G_0 in Figs. 3 and 4 can be qualitatively explained via the aspect of the linear band structure of graphene normal metal and the electron-hole conversion processes at different Fermi energies, as shown in Fig. 2. For the case of $\mu < \Delta_{\text{gap}}$ as in Fig. 3, at zero bias $eV = 0$, the phase spaces for the incident electrons and reflected holes are identical to each other, giving rise to the maximum Andreev conductance. However, once eV is increased but still lower than μ, it is clear that the phase space of the hole band shrinks and results in a monotonic decline in G/G_0 until the bias reaches the Fermi energy $eV = \mu$, where there is no density of states for a reflected hole, leading to a conductance dip, as shown in Fig. 4. In the regime $eV < \mu$, a conduction-band electron is reflected as a conduction-band hole via the Andreev reflection; it is called the intraband Andreev reflection (or Andreev retroreflection). Once the bias exceeds the Fermi energy $eV > \mu$, the incident electrons from the conduction band are converted as valence-band holes, leading to the interband Andreev reflection (or Andreev specular reflection). For this case, G/G_0 increases again with increasing eV due to the increase in phase space in the hole band. At $eV \gg \Delta_{\text{gap}}$, the tunneling process returns to the normal-metal-normal-metal tunneling, and the Andreev conductance saturates. Apparently, the Fermi energy serves as the "critical energy" for the transition between the intra- to interband Andreev reflection. On the contrary, only the Andreev retroreflection process exists as $\Delta_{\text{gap}} < \mu$, leading to a monotonic decline of G/G_0, as shown in Fig. 4.

In the following, we discuss the normalized conductance for the situation of nonzero barrier $\delta t \neq 0$. The vanishing of G/G_0 for the case of $\delta t = -t$ signifies no electron tunneling,

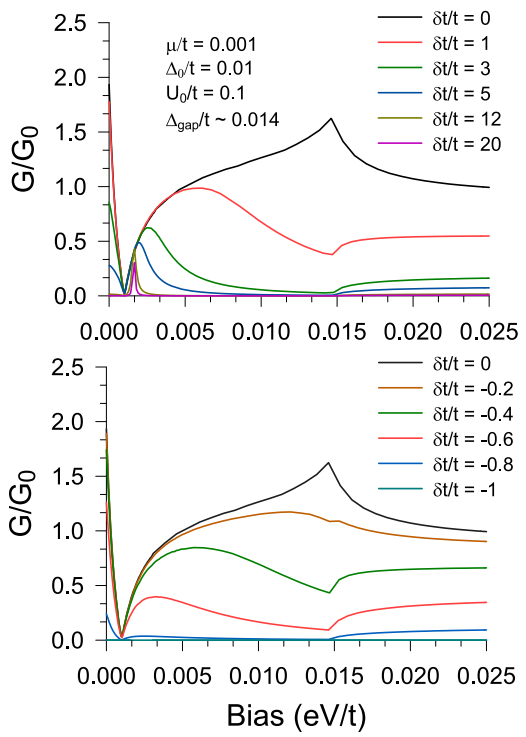

FIG. 3. The Andreev conductance of a graphene $d+id'$ superconducting junction with varying barrier heights $\delta t/t$ and fixed Fermi energy $\mu/t = 0.001$ and superconducting pairing strength $\Delta_0/t = 0.01$ and $U_0/t = 0.1$. The superconducting gap energy is around $\Delta_{\text{gap}}/t = 0.014$.

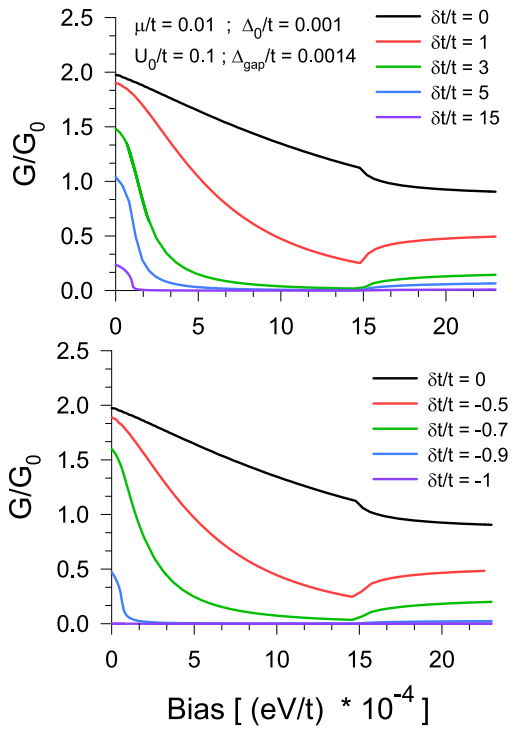

FIG. 4. The normalized Andreev conductance G/G_0 with varying barrier height $\delta t/t$ and fixed Fermi level $\mu/t = 0.01$ and superconducting pairing strength $\Delta_0/t = 0.001$. The superconducting gap energy is found to be $\Delta_{\text{gap}}/t = 0.0014$.

as expected. For the situation of a finite-potential barrier, our results qualitatively capture the most significant features of Andreev conductance in the presence of the δ barrier: In Figs. 3 and 4, as the barrier strength $\delta t/t$ is increased, G/G_0 dramatically decreases down to zero due to heavy scattering of electrons by the potential barrier, in good agreement with the previous results for the case of the 1D metal/s-wave N/SC junction in Ref. [2]. The cusps for the normalized conductance in Fig. 3 at $eV < \Delta_{\text{gap}}$ with nonzero δt can be simply understood as the competition between the graphene density of states and the effect of the δ barrier: The density of states for graphene at low energy is linearly proportional to the excitation energy, signifying that increasing the energy will enhance the conductance. On the contrary, the effect of δt tends to suppress the conductance. Therefore, the competition between the density of states and the δ barrier gives rise to the cusps in Fig. 3.

III. AR ACROSS A KANE-MELE/$(d+id')$-WAVE N/SC JUNCTION

In the past few decades, much effort has been devoted to searching for novel topological states of matters. The two examples of particular interest are topological insulators [29,30], which have insulating bulk states while the edge or surface supports time-reversal symmetry-protected conducting states, and topological superconductors, which support gapless, charged neutral Majorana edge (or surface) states [31] with superconducting bulk states.

Recently, the doped Kane-Mele (KM) model, which was originally proposed in Refs. [32,33], with large on-site electron-electron repulsive interaction on a 2D periodic honeycomb lattice was theoretically shown to feature a time-reversal-broken $(d_{x^2-y^2}+id_{xy})$-wave superconducting state in the bulk via renormalized mean-field theory [22,23]. Moreover, it was also found that the system undergoes a topological phase transition from the helical superconducting to the chiral superconducting order as the strength of the intrinsic spin-orbit coupling is decreased, and two pairs of counterpropagating helical Majorana zero modes were found theoretically at the edges of a finite-sized zigzag ribbon of the tight-binding KM t-J model in spite of the time-reversal-broken $(d_{x^2-y^2}+id_{xy})$-wave superconducting order [18,19]. Via the numerical simulation by density functional theory, the KM t-J model may be realized via doping adatoms such as indium or thallium on a graphene sheet, which generates an effective Kane-Mele-type intrinsic SO coupling ($\sim$20 meV) [34], which is larger than the undoped graphene. Besides graphene-based systems, our model is also applicable to other compounds with an underlying honeycomb lattice such as $In_3Cu_2VO_9$ [24,35–37], β-$Cu_2V_2O_7$ [38,39], MoS_2 [40], and silicene [41]. Those materials have been proposed to exhibit a chiral d-wave superconducting state around half filling. These exotic features discovered in the KM t-J model motivate us to seek the corresponding experimental signatures.

In the following, we investigate the Andreev reflection across a N/SC junction with the normal side being modeled by the doped KM model while the SC region is a doped correlated KM t-J model with $(d+id')$-wave spin-singlet superconducting order. The Kane-Mele model, which can be viewed as a spinful Haldane model [42], is composed of the

nearest-neighbor (NN) tight-binding Hamiltonian H_0 as in Eq. (1) and the next-nearest-neighbor (NNN) hopping intrinsic SO interaction H_{SO}:

$$\begin{aligned} H_{KM} &= H_O + H_{SO} + H_\mu, \\ H_{SO} &= i\lambda_{SO} \sum_{\ll i,j \gg} \sum_{\sigma,\sigma'=\uparrow\downarrow} \nu_{ij} \sigma^z_{\alpha\alpha'} c^\dagger_{i\alpha} c_{j\alpha'}, \\ H_\mu &= -\mu \sum_{i,\sigma} c^\dagger_{i\sigma} c_{i\sigma}. \end{aligned} \tag{24}$$

Here, $c_{i\sigma}$ ($c^\dagger_{i\sigma}$) annihilates (creates) an electron on either the A or B sublattice on the ith unit cell. $\ll i,j \gg$ denotes the NNN indices, λ_{SO} is the coupling strength of the intrinsic SO interaction, and $\sigma, \sigma' = \uparrow, \downarrow$ represent spins. $\nu_{ij} = \pm 1$ is an orientation-dependent factor: $\nu_{ij} = 1$ for an electron making a right turn while moving from the ith site to the jth NNN site, and $\nu_{ij} = -1$ for a left turn. The doping is characterized by H_μ, with μ being the value of the chemical potential. The mean-field Hamiltonian on a periodic lattice in terms of the basis $\Psi_{\boldsymbol{k}} = (c^\uparrow_{A,\boldsymbol{k}}\, c^\uparrow_{B,\boldsymbol{k}}, c^\downarrow_{A,\boldsymbol{k}}\, c^\downarrow_{B,\boldsymbol{k}}, c^{\uparrow\dagger}_{A,-\boldsymbol{k}}\, c^{\uparrow\dagger}_{B,-\boldsymbol{k}}, c^{\downarrow\dagger}_{A,-\boldsymbol{k}}\, c^{\downarrow\dagger}_{B,-\boldsymbol{k}})^T$ is given by the 8×8 matrix

$$\begin{aligned} \mathcal{H}_{\boldsymbol{k}} &= \begin{pmatrix} h^+_{\boldsymbol{k}} - \mu & 0 & 0 & \Delta_{\boldsymbol{k}} \\ 0 & h^-_{\boldsymbol{k}} - \mu & -\Delta_{\boldsymbol{k}} & 0 \\ 0 & -\Delta^\dagger_{\boldsymbol{k}} & \mu - h^{+*}_{-\boldsymbol{k}} & 0 \\ \Delta^\dagger_{\boldsymbol{k}} & 0 & 0 & \mu - h^{-*}_{-\boldsymbol{k}} \end{pmatrix} \\ &= \begin{pmatrix} h^+_{\boldsymbol{k}} - \mu & 0 & 0 & \Delta_{\boldsymbol{k}} \\ 0 & h^-_{\boldsymbol{k}} - \mu & -\Delta_{\boldsymbol{k}} & 0 \\ 0 & -\Delta^\dagger_{\boldsymbol{k}} & \mu - h^-_{\boldsymbol{k}} & 0 \\ \Delta^\dagger_{\boldsymbol{k}} & 0 & 0 & \mu - h^+_{\boldsymbol{k}} \end{pmatrix}, \end{aligned} \tag{25}$$

with

$$h^\pm_{\boldsymbol{k}} = \begin{pmatrix} \pm\gamma(\boldsymbol{k}) & f(\boldsymbol{k}) \\ f^*(\boldsymbol{k}) & \mp\gamma(\boldsymbol{k}) \end{pmatrix}, \tag{26}$$

$$\gamma(\boldsymbol{k}) = 2\lambda_{SO}\left[2\cos\frac{3k_x}{2}\sin\frac{\sqrt{3}k_y}{2} - \sin\sqrt{3}k_y\right]. \tag{27}$$

In the second line of Eq. (25), we have applied the relations of $\gamma(-\boldsymbol{k}) = -\gamma(\boldsymbol{k})$ [43] and $f^*(\boldsymbol{k}) = f(-\boldsymbol{k})$.

The electronic excitations near the $\boldsymbol{K}_\tau$ valley on the N and SC sides are described by the linearized DBdG equations, which take the form

$$\begin{pmatrix} \mathcal{H}_\tau(\boldsymbol{q}) - \mu & \Theta(x)\bar{\Delta}_\tau(\boldsymbol{q}) \\ \Theta(x)\bar{\Delta}_\tau(\boldsymbol{q})^\dagger & \mu - \mathcal{H}_\tau(\boldsymbol{q}) \end{pmatrix} \begin{pmatrix} u_\tau \\ v_\tau \end{pmatrix} = \frac{\epsilon_q}{t} \begin{pmatrix} u_\tau \\ v_\tau \end{pmatrix}. \tag{28}$$

Here, $(u_\tau, v_\tau) = (u^\uparrow_{A\tau}, u^\uparrow_{B\tau}, u^\downarrow_{A\tau}, u^\downarrow_{B\tau}, v^\uparrow_{A\tau}, v^\uparrow_{B\tau}, v^\downarrow_{A\tau}, v^\downarrow_{B\tau})^T$ is an eight-component wave function in the momentum domain near the $\boldsymbol{K}_\tau$ valley, with the first four components u_τ being for particles and the last four components v_τ being for holes.

$$\begin{aligned} \mathcal{H}_\tau(\boldsymbol{q}) = &-\sigma_0(\pi^x q_y + \tau\pi^y q_x) - 3\sqrt{3}\,\lambda(x)\,\tau\sigma^z\pi^z \\ &-(U_0/t)\sigma^0\pi^0\Theta(x), \end{aligned} \tag{29}$$

where the 2×2 unit matrix $\sigma^0 = \mathrm{diag}(1,1)$ and the three Pauli matrices $\sigma^{x,y,z}$ are for the spin subspace in the Hilbert space, while the matrices π are for the sublattices already defined in Eqs. (5) and (6). Here, we assume the magnitudes of intrinsic SO coupling in the N and the SC regions can be adjusted independently; thus, we introduce

$$\lambda(x) = \begin{cases} \lambda_{SO}/t, & x < 0, \\ \lambda'_{SO}/t, & x > 0, \end{cases} \tag{30}$$

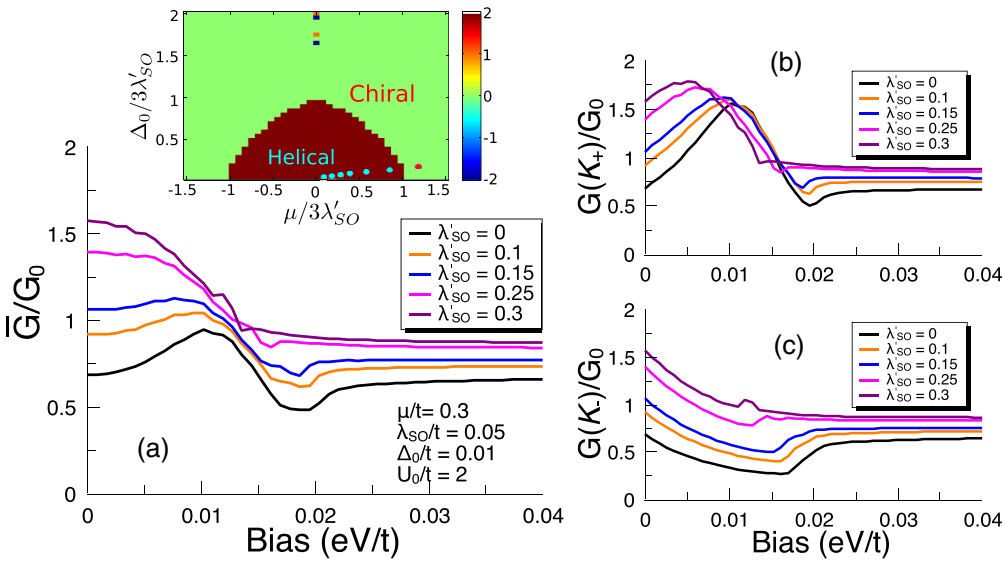

FIG. 5. (a) shows the average normalized Andreev conductance $\bar{G}/G_0$ across a KM $d + id'$-wave N/SC junction in terms of varying the intrinsic SO coupling λ'_{SO} in the SC side in the absence of local strain. Here, we fix the Fermi energy $\mu/t = 0.3$, the intrinsic SO coupling $\lambda_{SO}/t = 0.05$ in the N region, the electrostatic potential $U_0/t = 2$ in the SC, and the value of SC pairing $\Delta_0/t = 0.01$. The inset illustrates the topological phase diagram for the bulk state in the SC region, showing that the bulk will undergo the chiral (green area) to helical (brown area) topological transition as the ratio Δ_0/λ'_{SO} or μ/λ'_{SO} is varied. The color bar represents the value of the spin-Chern number. (b) and (c) show the normalized Andreev conductance $G(K_+)/G_0$ and $G(K_-)/G_0$ contributions from the electrons from the $\boldsymbol{K}_+$ and $\boldsymbol{K}_-$ valleys, respectively.

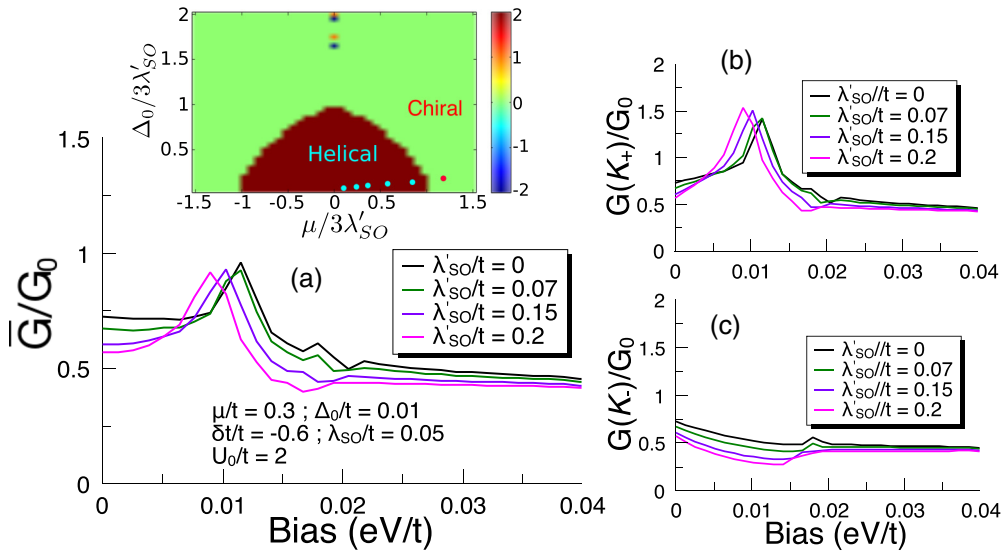

FIG. 6. (a) shows the average Andreev conductance $\bar{G}/G_0$ in the presence of a constant δ-gauge field with barrier strength $\delta t/t = -0.6$ at the interface, while (b) and (c) show the Andreev conductance $G(K_\pm)/G_0$ from the $\boldsymbol{K}_\pm$ valleys, respectively. All the remaining parameters are the same as those in Fig. 5.

where λ_{SO} indicates the intrinsic SO coupling in N and λ'_{SO} indicates that in SC. Here, $\bar{\Delta}_\tau(\boldsymbol{q})$ is a 4×4 matrix for the linearized $(d+id')$-wave pairing near the $\boldsymbol{K}_\tau$ Dirac point, which takes the form

$$\bar{\Delta}_\tau(\boldsymbol{q}) \equiv \begin{pmatrix} 0 & \Delta_\tau(\boldsymbol{q}) \\ -\Delta_\tau(\boldsymbol{q}) & 0 \end{pmatrix}. \tag{31}$$

Around $\boldsymbol{K}_-$, $\Delta_-(\boldsymbol{q})$ is given by Eq. (16) in the previous section, which is related to the one for the $\boldsymbol{K}_+$ valley by $\Delta_+(\boldsymbol{q}) = \Delta_-^T(-\boldsymbol{q})$.

Because the KM t-J model exhibits an effective spin-singlet $p \pm ip'$ superconducting order near the two Dirac points $\boldsymbol{K}_\pm$ [19], the valley degeneracy no longer exists, and we ought to consider the normalized Andreev conductance contributed from $\boldsymbol{K}_+$ and $\boldsymbol{K}_-$. Here, we assume the electron scattering occurs within only one valley; thus, the normalized Andreev conductance can be simply evaluated by taking the average of the individual contributions from $\boldsymbol{K}_\pm$. The Andreev conductance contributed from one valley can be similarly obtained via the BTK formalism. The average of the normalized Andreev conductance is expressed as

$$\frac{\bar{G}}{G_0} = \frac{1}{G_0}\frac{G(K_+)+G(K_-)}{2}, \tag{32}$$

where $G(K_\pm)$ is the Andreev conductance from $\boldsymbol{K}_\pm$, respectively. The results are illustrated in Figs. 5 and 6.

In the following, we qualitatively discuss the conductance behaviors for Figs. 5 and 6. As the δ barrier is switched off, the Andreev conductance $G(K_-)$ from the $\boldsymbol{K}_-$ valley, as shown in Fig. 5(c), monotonically decreases with the increasing bias eV due to the shrinking of the phase space in the hole band, as shown in Fig. 7. The resulting behavior of the Andreev conductance $G(K_-)$ is similar to the case in Fig. 4; hence, only the Andreev retroreflection process is involved. Due to the inversion symmetry breaking in the KM t-J model, the Andreev conductance $G(K_+)$ from $\boldsymbol{K}_+$ in Fig. 5(b) behaves entirely different from $G(K_-)$. Averaging $G(K_+)$ and $G(K_-)$ gives rise to distinctive Andreev conductance behaviors for different values of λ'_{SO}. For small intrinsic SO coupling, we find that the average Andreev conductance $\bar{G}/G_0$ increases as the bias is increased at low bias, where $\bar{G}/G_0$ behaves in a manner similar to the Andreev specular reflection. On the contrary, for large intrinsic SO coupling λ'_{SO}, $\bar{G}/G_0$ monotonically decreases with increasing bias. We argue the Andreev retroreflection may dominate $\bar{G}/G_0$ in this situation.

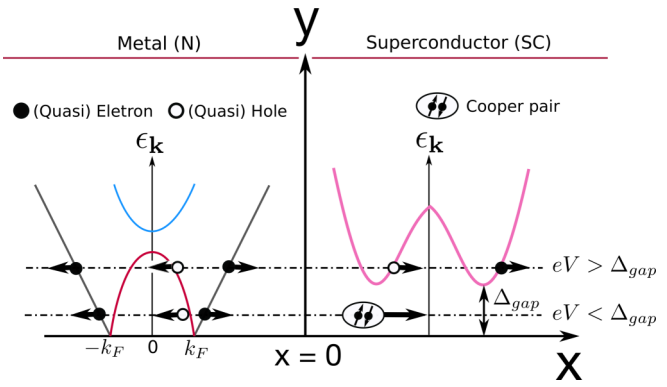

FIG. 7. The band structure in the left region is for the Kane-Mele model near the Dirac points. Due to the intrinsic SO coupling, we can see a band gap between the conduction (red solid line) and valence (blue solid line) hole bands.

IV. DISCUSSION AND CONCLUSION

Before we conclude, the effect of electron scattering by the edge states on the Andreev conductance deserves some discussion here. As mentioned in the previous section, via the bulk-edge correspondence [30,44], the KM t-J model supports chiral or helical Majorana edge states depending on the topological phase in the bulk. Accordingly, we

anticipate that as the electron scattering by the quasiparticles in the edge states at the N/SC interface is considered, the Andreev conductance may exhibit distinctive behavior rather than a relatively smooth crossover as the SC region is tuned to undergo a chiral-to-helical topological phase transition. We expect this distinctive behavior of the Andreev conductance at the topological critical point could serve as an experimental signature to probe the topological phase transition.

In conclusion, we have investigated the Andreev reflection based on Blonder-Tinkham- Klapwijk formalism in a graphene normal-metal/$(d+id')$-wave superconducting junction with a finite barrier on the N/SC interface. In order to investigate the electron scatterings on a N/SC junction with different transparencies, an effective Dirac δ-gauge potential is introduced by adding a homogeneous local strain parallel to the interface. In the absence of local strain, i.e., $\delta t = 0$, our results successfully reproduce the normalized Andreev conductance G/G_0 curves in Ref. [6]. At the other extreme parameter regime of $\delta t = -t$, the Andreev conductance vanishes because the N/SC junction is disconnected and therefore electron tunneling is forbidden. For a finite barrier, the Andreev conductance dramatically decreases down to zero as the barrier strength δt is increased. Despite the different mechanisms of the barrier on the junction, the qualitative behaviors of the conductance in our case resemble the effect of a potential barrier at the interface of a conventional 1D N/SC junction in the BTK framework, indicating that a homogeneous narrow local strain on a junction tends to suppress the Andreev conductance.

We further investigated the Andreev reflection across the N/SC junction with the N region being described by the doped Kane-Mele model, while the SC region features $(d+id')$-wave spin-singlet pairing induced by strong electron correlations. The normalized Andreev conductance contributed by the $\boldsymbol{K}_+$ and $\boldsymbol{K}_-$ valleys illustrates entirely different behaviors due to the different effective superconducting pairing symmetries near the two Dirac points. Our results provide spectra of the normalized Andreev conductance within certain parameter regimes for future experiments.

ACKNOWLEDGMENTS

This work was supported by the Ministry of Science and Technology (MoST), Taiwan. We also acknowledge support from TCECM and the Academia Sinica Research Program on Nanoscience and Nanotechnology, Taiwan. This work was also supported by MOST Grant No. 104-2112-M-009-004-MY3, the MOE-ATU program, and the NCTS of Taiwan, Republic of China (C.H.C.).

APPENDIX A: BOUNDARY CONDITIONS FOR THE GRAPHENE N/N JUNCTION WITH A δ-GAUGE FIELD

In this Appendix, we repeat the derivations of the boundary conditions for the electronic transport through a graphene normal-metal-normal-metal (N/N) junction in the low-energy limit with an effective δ-gauge field in between. This issue was originally addressed by Castro Neto *et al.* [16,17].

1. For the $\boldsymbol{K}_-$ valley

Schrodinger's equations for the graphene tight-binding model in the low-energy limit near the $\boldsymbol{K}_-$ valley read

$$-[\pi^y(-i\partial_x)-\pi^x(-i\partial_y+\mathcal{A}_y)]\Psi_-(\boldsymbol{r})=(\epsilon/t)\,\Psi_-(\boldsymbol{r})$$
$$\Rightarrow\begin{bmatrix}0 & -\partial_x+i\partial_y-\mathcal{A}_y\\ \partial_x+i\partial_y-\mathcal{A}_y & 0\end{bmatrix}\Psi_-(\boldsymbol{r})=-(\epsilon/t)\,\Psi_-(\boldsymbol{r}). \tag{A1}$$

Expressing the two-component wave function as $\Psi_-(\boldsymbol{r})=(\psi'_A(\boldsymbol{r}),\psi'_B(\boldsymbol{r}))^T$ and substituting the effective δ potential of $\mathcal{A}_y$ in Eq. (A1) yields

$$\Rightarrow\begin{cases}[-\partial_x+i\partial_y+\frac{\delta t}{t}\delta(x)]\psi'_B(\boldsymbol{r})=-(\epsilon/t)\,\psi'_A(\boldsymbol{r}),\\ [\partial_x+i\partial_y+\frac{\delta t}{t}\delta(x)]\psi'_A(\boldsymbol{r})=-(\epsilon/t)\,\psi'_B(\boldsymbol{r}).\end{cases} \tag{A2}$$

Integrating Schrodinger's equations in Eq. (A1) over an infinitesimal region across the origin, i.e., $\int_{0-}^{0+}dx$, we obtain the boundary condition

$$\Rightarrow\begin{cases}\psi'_B(0^-)+\frac{\delta t}{t}\,\psi'_B(0)=\psi'_B(0^+),\\ \psi'_A(0^+)+\frac{\delta t}{t}\,\psi'_A(0)=\psi'_A(0^-).\end{cases} \tag{A3}$$

Since Schrodinger's equations with a linear Dirac spectrum are first order differential equations, we cannot require the wave function to be continuous at the origin, giving rise to the wave-function ambiguity, $\psi'_A(0)$ and $\psi'_B(0)$, as we see in Eq. (A3). Here, we choose the undetermined wave functions in following the way:

$$\psi'_B(0)=\psi'_B(0^-),\quad \psi'_A(0)=\psi'_A(0^+), \tag{A4}$$

and Eq. (A3) becomes

$$\Rightarrow\begin{cases}\psi'_B(0^+)=\eta\,\psi'_B(0^-),\\ \psi'_A(0^-)=\eta\,\psi'_A(0^+).\end{cases} \tag{A5}$$

Later, we will show that the choice of the undetermined wave functions at $x=0$ in Eq. (A4) leads to the conservation of the probability current. Thus, current conservation justifies our choice of the undetermined wave functions.

We may imagine that an incident electron far from the interface in the graphene sheet in the region of $x<0$ moves toward the interface and gets scattered with the potential at the origin. By solving Schrodinger's equation, the right-moving state in $\boldsymbol{q}$ space for the incident electron is given by

$$\tilde{\Psi}_-(q_x,q_y)=\frac{1}{\sqrt{2}}\begin{pmatrix}-\frac{iq_x+q_y}{q}\\ -1\end{pmatrix}=-\frac{e^{i\phi}}{\sqrt{2}}\begin{pmatrix}1\\ e^{-i\phi}\end{pmatrix}, \tag{A6}$$

while the left-moving state for the reflected electron can be obtained by simply reversing the sign of q_x in Eq. (A6), which is given by

$$\tilde{\Psi}_-(-q_x,q_y)=\frac{1}{\sqrt{2}}\begin{pmatrix}\frac{iq_x-q_y}{q}\\ -1\end{pmatrix}=-\frac{e^{-i\phi}}{\sqrt{2}}\begin{pmatrix}1\\ e^{i\phi}\end{pmatrix}. \tag{A7}$$

The total wave functions with a normalized incident state on the left and right sides of the graphene sheet are

$$\Psi_-^L(\boldsymbol{r})=e^{iq_xx+iq_yy}\,\tilde{\Psi}_-(q_x,q_y)+\mathcal{R}\,e^{-iq_xx+iq_yy}\,\tilde{\Psi}_-(-q_x,q_y), \tag{A8}$$

$$\Psi_-^R(\boldsymbol{r})=\mathcal{T}\,e^{iq_xx+iq_yy}\,\tilde{\Psi}_-(q_x,q_y), \tag{A9}$$

with $\mathcal{R}$ and $\mathcal{T}$ being the reflection and transmission coefficients. Here, the superscripts L and R stand for left and right, respectively. The boundary conditions are given by

$$\mathcal{T}e^{-i\phi} = \eta(e^{-i\phi} + Re^{i\phi}), \quad 1 + \mathcal{R} = \eta\,\mathcal{T}. \tag{A10}$$

$\mathcal{R}$ and $\mathcal{T}$ are found to be

$$\mathcal{T} = \eta\,\frac{1 - e^{2i\phi}}{1 - \eta^2\,e^{2i\phi}}, \quad \mathcal{R} = \frac{\eta^2 - 1}{1 - \eta^2\,e^{2i\phi}}. \tag{A11}$$

Apparently, $\mathcal{T} = 0$ when $\eta = 0$, as expected, and the probability current is conserved; that is, $|\mathcal{R}|^2 + |\mathcal{T}|^2 = 1$.

2. For the K_+ valley

Likewise, the Schrodinger equations for the $\boldsymbol{K}_+ = (0, -\frac{4\pi}{3\sqrt{3}})$ valley are given by

$$[\pi^{y*}(-i\partial_x) - \pi^x(-i\partial_y - \mathcal{A}_y)]\Psi_+(\mathbf{r}) = (\epsilon/t)\,\Psi_+(\mathbf{r})$$
$$\Rightarrow \begin{bmatrix} 0 & \partial_x + i\partial_y + \mathcal{A}_y \\ -\partial_x + i\partial_y + \mathcal{A}_y & 0 \end{bmatrix}\Psi_+(\mathbf{r}) = (\epsilon/t)\,\Psi_+(\mathbf{r}). \tag{A12}$$

Expressing $\Psi_+(\mathbf{r}) = (\psi_A(\mathbf{r}), \psi_B(\mathbf{r}))^T$, we have

$$\Rightarrow \begin{cases} (\partial_x + i\partial_y + \mathcal{A}_y)\psi_B(\mathbf{r}) = (\epsilon/t)\,\psi_A(\mathbf{r}), \\ (-\partial_x + i\partial_y + \mathcal{A}_y)\psi_A(\mathbf{r}) = (\epsilon/t)\,\psi_B(\mathbf{r}). \end{cases} \tag{A13}$$

Next, integrating from $x = 0^-$ to $x = 0^+$ yields the boundary conditions

$$\Rightarrow \begin{cases} \psi_B(0^+) - \psi_B(0^-) = \frac{\delta t}{t}\,\psi_B(0), \\ \psi_A(0^-) - \psi_A(0^+) = \frac{\delta t}{t}\,\psi_A(0). \end{cases} \tag{A14}$$

We can immediately see the undetermined wave functions $\psi_A(0)$ and $\psi_B(0)$ appear on the right-hand side of Eq. (A14). For the same reason of current conservation, we choose the undetermined wave function to be

$$\psi_B(0) = \psi_B(0^-), \quad \psi_A(0) = \psi_A(0^+). \tag{A15}$$

Note that due to the relation of the time-reversal partner for the states near the $\boldsymbol{K}_+$ and $\boldsymbol{K}_-$ wave vectors, the choice of the undetermined wave functions at $x = 0$ in Eq. (A15) is identical to that in Eq. (A4).

To calculate the transmission and reflection coefficients, we first prepare the normalized right-moving and left-moving states for the incident and reflected electrons in the momentum space:

$$\tilde{\Psi}_+(q_x, q_y) = \frac{1}{\sqrt{2}}\begin{pmatrix} \frac{iq}{q_x - iq_y} \\ 1 \end{pmatrix} = -\frac{e^{-i\phi}}{\sqrt{2}}\begin{pmatrix} 1 \\ -e^{i\phi} \end{pmatrix},$$
$$\tilde{\Psi}_+(-q_x, q_y) = \frac{1}{\sqrt{2}}\begin{pmatrix} -\frac{iq_x + q_y}{q} \\ 1 \end{pmatrix} = -\frac{e^{i\phi}}{\sqrt{2}}\begin{pmatrix} 1 \\ -e^{-i\phi} \end{pmatrix}. \tag{A16}$$

The phase ϕ is defined in the way shown in Fig. 8. The total wave function on the left-hand side, denoted as $\Psi_+^L(\boldsymbol{r})$, can be expressed as a superposition of the incident and reflected wave functions, namely,

$$\Psi_+^L(\boldsymbol{r}) = e^{ik_x x + ik_y y}\tilde{\Psi}_+(q_x, q_y) + \mathcal{R}\,e^{-ik_x x + ik_y y}\,\tilde{\Psi}_+(-q_x, q_y). \tag{A17}$$

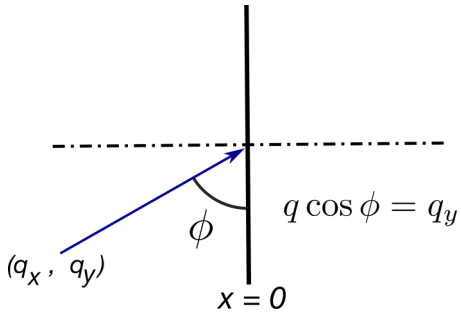

FIG. 8. The incident angle as a function of the quasimomentum $\boldsymbol{q}$ for incident electrons.

The total wave function on the right-hand side $\Psi_+^R(\boldsymbol{r})$ is given by

$$\Psi_+^R(\boldsymbol{r}) = \mathcal{T}\,e^{ik_x x + ik_y y}\tilde{\Psi}_+(q_x, q_y). \tag{A18}$$

In the above, we neglect the phase factor and prefactor $1/\sqrt{2}$ since it will play no role in finding $\mathcal{R}$ and $\mathcal{T}$. Written $\eta = 1 + \delta t/t$, the boundary conditions can be found to be

$$\Rightarrow \begin{cases} \mathcal{T}e^{i\phi} = \eta(e^{i\phi} + \mathcal{R}\,e^{-i\phi}), \\ 1 + \mathcal{R} = \eta\mathcal{T}. \end{cases} \tag{A19}$$

We can solve for the transmission and reflection coefficients:

$$\mathcal{T} = \eta\,\frac{1 - e^{-2i\phi}}{1 - \eta^2 e^{-2i\phi}}, \quad \mathcal{R} = \frac{1 - \eta^2}{\eta^2 e^{-2i\phi} - 1}. \tag{A20}$$

We can immediately check that once $\eta = 0\,(\delta t = -t)$, there are no transmitted particles since the graphene has been cut into two separate pieces, and the probability current is conserved, that is, $|\mathcal{R}|^2 + |\mathcal{T}|^2 = 1$.

APPENDIX B: THE BOUNDARY CONDITIONS FOR THE KANE-MELE $d + id'$ N/SC JUNCTION

In this section, we derive the boundary conditions for the electron scattering across the Kane-Mele $(d + id')$-wave superconducting N/SC junction in the presence of a δ barrier for the $\boldsymbol{K}_\pm$ valleys.

The wave function for the DBdG Hamiltonian for the $\boldsymbol{K}_-$ valley can be written as $\Psi(x, y) = (f_{A\uparrow}, f_{B\uparrow}, f_{A\downarrow}, f_{B\downarrow}, g_{A\uparrow}, g_{B\uparrow}, g_{A\downarrow}, g_{B\downarrow})$. In real space, the DBdG equations with eigenenergy ϵ are given by

$$\partial_x f_{B\uparrow}(x) - \frac{3\Delta_0}{2t}\,\partial_x g_{B\downarrow}(x) - \frac{\delta t}{t}\,\delta(x) f_{B\uparrow}(x) = (\epsilon/t) f_{A\uparrow}(x),$$
$$-\partial_x f_{A\uparrow}(x) + \frac{3\Delta_0}{2t}\,g_{A\downarrow}(x) - \frac{\delta t}{t}\delta(x)\,f_{A\uparrow}(x) = (\epsilon/t) f_{B\uparrow}(x),$$
$$\partial_x f_{B\downarrow}(x) + \frac{3\Delta_0}{2t}\,\partial_x g_{B\uparrow}(x) - \frac{\delta t}{t}\delta(x)\,f_{B\downarrow}(x) = (\epsilon/t) f_{A\downarrow}(x),$$
$$-\partial_x f_{A\downarrow}(x) - \frac{\delta t}{t}\delta(x)\,f_{A\downarrow}(x) = (\epsilon/t) f_{B\downarrow}(x),$$
$$-\partial_x g_{B\uparrow}(x) + \frac{\delta t}{t}\delta(x) g_{B\uparrow}(x) = (\epsilon/t)\,g_{A\uparrow}(x),$$
$$\partial_x g_{A\uparrow}(x) - \frac{3\Delta_0}{2t}\,\partial_x f_{A\downarrow}(x) + \frac{\delta t}{t}\delta(x)\,g_{A\uparrow}(x) = (\epsilon/t)\,g_{B\uparrow}(x),$$

$$-\partial_x g_{B\downarrow}(x) + \frac{\delta t}{t}\delta(x) g_{B\downarrow}(x) = (\epsilon/t)\, v_{A\downarrow}(x),$$
$$\partial_x g_{A\downarrow}(x) + \frac{3\Delta_0}{2t}\,\partial_x f_{A\uparrow}(x) + \frac{\delta t}{t}\delta(x)\, g_{A\downarrow}(x) = (\epsilon/t)\, g_{B\downarrow}(x). \tag{B1}$$

We integrate the above equations over an infinitesimal distance across the interface, and Eq. (B1) becomes

$$\begin{aligned}
\left[f^{sc}_{B\uparrow}(0) - f^{N}_{B\uparrow}(0)\right] - \frac{3\Delta_0}{2t}\left[g^{sc}_{B\downarrow}(0) - g^{N}_{B\downarrow}(0)\right] &= \frac{\delta t}{t} f_{B\uparrow}(0),\\
-\left[f^{sc}_{A\uparrow}(0) - f^{N}_{A\uparrow}(0)\right] &= \frac{\delta t}{t} f_{A\uparrow}(0),\\
\left[f^{sc}_{B\downarrow}(0) - f^{N}_{B\downarrow}(0)\right] + \frac{3\Delta_0}{2t}\left[g^{sc}_{B\uparrow}(0) - g^{N}_{B\uparrow}(0)\right] &= \frac{\delta t}{t} f_{B\downarrow}(0),\\
-\left[f^{sc}_{A\downarrow}(0) - f^{N}_{A\downarrow}(0)\right] &= \frac{\delta t}{t} f_{A\downarrow}(0),\\
\left[g^{sc}_{B\uparrow}(0) - g^{N}_{B\uparrow}(0)\right] &= \frac{\delta t}{t} g_{B\uparrow}(0),\\
\left[g^{sc}_{A\uparrow}(0) - g^{N}_{A\uparrow}(0)\right] - \frac{3\Delta_0}{2t}\left[f^{sc}_{A\downarrow}(0) - f^{N}_{A\downarrow}(0)\right] &= -\frac{\delta t}{t} g_{A\uparrow}(0),\\
\left[g^{sc}_{B\downarrow}(0) - g^{N}_{B\downarrow}(0)\right] &= \frac{\delta t}{t} g_{B\downarrow}(0),\\
\left[g^{sc}_{A\downarrow}(0) - g^{N}_{A\downarrow}(0)\right] + \frac{3\Delta_0}{2t}\left[f^{sc}_{A\uparrow}(0) - f^{N}_{A\uparrow}(0)\right] &= \frac{\delta t}{t} g_{A\downarrow}(0).
\end{aligned} \tag{B2}$$

In the above equations for the boundary conditions, $f_{\alpha\sigma}(0^+) \equiv f^{sc}_{\alpha\sigma}$ and $f_{\alpha\sigma}(0^-) \equiv f^{N}_{\alpha\sigma}$, where α denotes the A or B sublattice and σ denotes the spin $\sigma = \uparrow, \downarrow$. Similarly, the wave-function ambiguity at $x = 0$ also exists in Eq. (B2) because the DBdG equations are first order differential equations. Following a similar approach, we are able to determine $\Psi(0)$ via the requirements of no tunneling current across the N/SC junction as $\Delta_0 = 0$ and $\delta t = -t$. Based on Eq. (21), the boundary conditions at $x = 0$ can be written as

$$\begin{aligned}
f^{sc}_{B\uparrow}(0) &= \eta\, f^{N}_{B\uparrow}(0) + \frac{3\Delta_0}{2t}\left[g^{sc}_{B\downarrow}(0) - g^{N}_{B\downarrow}(0)\right],\\
f^{N}_{A\uparrow}(0) &= \eta\, f^{sc}_{A\uparrow}(0),\\
f^{sc}_{B\downarrow}(0) &= \eta\, f^{N}_{B\downarrow}(0) - \frac{3\Delta_0}{2t}\left[g^{sc}_{B\uparrow}(0) - g^{N}_{B\uparrow}(0)\right],\\
f^{N}_{A\downarrow}(0) &= \eta\, f^{sc}_{A\downarrow}(0),\\
g^{sc}_{B\uparrow}(0) &= \eta\, g^{N}_{B\uparrow}(0),\\
g^{N}_{A\uparrow}(0) &= \eta\, g^{sc}_{A\uparrow}(0) - \frac{3\Delta_0}{2t}\left[f^{sc}_{A\downarrow}(0) - f^{N}_{A\downarrow}(0)\right],\\
g^{sc}_{B\downarrow}(0) &= \eta\, g^{N}_{B\downarrow}(0),\\
g^{N}_{A\downarrow}(0) &= \eta\, g^{sc}_{A\downarrow}(0) + \frac{3\Delta_0}{2t}\left[f^{sc}_{A\uparrow}(0) - f^{N}_{A\uparrow}(0)\right],
\end{aligned} \tag{B3}$$

where $\eta \equiv 1 + \delta t/t$. Following the same procedures, the boundary conditions for the $\boldsymbol{K}_+$ valley are given by

$$\begin{aligned}
f^{sc}_{B\uparrow}(0) &= \eta\, f^{N}_{B\uparrow}(0),\\
f^{N}_{A\uparrow}(0) &= \eta\, f^{sc}_{A\uparrow}(0) - \frac{3\Delta_0}{2t}\left[g^{sc}_{A\downarrow}(0) - g^{N}_{A\downarrow}(0)\right],\\
f^{sc}_{B\downarrow}(0) &= \eta\, f^{N}_{B\downarrow}(0),\\
f^{N}_{A\downarrow}(0) &= \eta\, f^{sc}_{A\downarrow}(0) + \frac{3\Delta_0}{2t}\left[g^{sc}_{A\uparrow}(0) - g^{N}_{A\uparrow}(0)\right],\\
g^{sc}_{B\uparrow}(0) &= \eta\, g^{N}_{B\uparrow}(0) + \frac{3\Delta_0}{2t}\left[f^{sc}_{B\downarrow}(0) - f^{N}_{B\downarrow}(0)\right],\\
g^{N}_{A\uparrow}(0) &= \eta\, g^{sc}_{A\uparrow}(0),\\
g^{sc}_{B\downarrow}(0) &= \eta\, g^{N}_{B\downarrow}(0) - \frac{3\Delta_0}{2t}\left[f^{sc}_{B\uparrow}(0) - f^{N}_{B\uparrow}(0)\right],\\
g^{N}_{A\downarrow}(0) &= \eta\, g^{sc}_{A\downarrow}(0).
\end{aligned} \tag{B4}$$

[1] A. F. Andreev, J. Exptl. Theoret. Phys. **46**, 1823 (1964) [Sov. Phys. JETP **19**, 1228 (1964)].
[2] G. E. Blonder, M. Tinkham, and T. M. Klapwijk, Phys. Rev. B **25**, 4515 (1982).
[3] C. W. J. Beenakker, Phys. Rev. Lett. **97**, 067007 (2006).
[4] C. Beenakker, Rev. Mod. Phys. **80**, 1337 (2008).
[5] B. Lv, C. Zhang, and Z. Ma, Phys. Rev. Lett. **108**, 077002 (2012).
[6] Y. Jiang, D. X. Yao, E. W. Carlson, H. D. Chen, and J. P. Hu, Phys. Rev. B **77**, 235420 (2008).
[7] T. Ludwig, Phys. Rev. B **75**, 195322 (2007).
[8] J. Linder and T. Yokoyama, Phys. Rev. B **89**, 020504(R) (2014).
[9] L. Majidi, H. Rostami, and R. Asgari, Phys. Rev. B **89**, 045413 (2014).
[10] L. Majidi and R. Asgari, Phys. Rev. B **93**, 195404 (2016).
[11] J. Linder, Y. Tanaka, T. Yokoyama, A. Sudbø, and N. Nagaosa, Phys. Rev. Lett. **104**, 067001 (2010).
[12] Y. Tanaka, Y. Mizuno, T. Yokoyama, K. Yada, and M. Sato, Phys. Rev. Lett. **105**, 097002 (2010).
[13] D. K. Efetov *et al.*, Nat. Phys. **12**, 328 (2016).
[14] M. R. Sahu, P. Raychaudhuri, and A. Das, Phys. Rev. B **94**, 235451 (2016).
[15] M. I. Katsnelson, K. S. Novoselov, and A. K. Geim, Nat. Phys. **2**, 620 (2006).
[16] V. M. Pereira and A. H. Castro Neto, Phys. Rev. Lett. **103**, 046801 (2009).
[17] A. H. Castro Neto, N. M. R. Peres, K. S. Novoselov, and A. K. Geim, Rev. Mod. Phys. **81**, 109 (2009).
[18] S. J. Sun, C. H. Chung, Y. Y. Chang, W. F. Tsai, and F. C. Zhang, Sci. Rep. **6**, 24102 (2016).
[19] S. M. Huang, W. F. Tsai, C. H. Chung, and C. Y. Mou, Phys. Rev. B **93**, 054518 (2016).
[20] P. Wallace, Phys. Rev. **71**, 622 (1947).
[21] H. B. Heersche, P. Jarillo-Herrero, J. B. Oostinga, L. M. K. Vandersypen, and A. F. Morpurgo, Nature (London) **446**, 56 (2007).
[22] A. M. Black-Schaffer and S. Doniach, Phys. Rev. B **75**, 134512 (2007).

[23] A. M. Black-Schaffer and C. Honerkamp, J. Phys. Condens. Matter **26**, 423201 (2014).
[24] W. Wu, M. M. Scherer, C. Honerkamp, and K. Le Hur, Phys. Rev. B **87**, 094521 (2013).
[25] M. Tinkham, *Introduction to Superconductivity* (McGraw-Hill, New York, 1975).
[26] P. G. de Gennes, *Superconductivity of Metals and Alloys* (Benjamin, New York, 1966).
[27] B. Uchoa and A. H. Castro Neto, Phys. Rev. Lett. **98**, 146801 (2007).
[28] H. Suzuura and T. Ando, Phys. Rev. Lett. **89**, 266603 (2002).
[29] X. L. Qi and S. C. Zhang, Rev. Mod. Phys. **83**, 1057 (2011).
[30] C. L. Kane and M. Z. Hasan, Rev. Mod. Phys. **82**, 3045 (2010).
[31] J. Alicea, Rep. Prog. Phys. **75**, 076501 (2012).
[32] C. L. Kane and E. J. Mele, Phys. Rev. Lett. **95**, 226801 (2005).
[33] C. L. Kane and E. J. Mele, Phys. Rev. Lett. **95**, 146802 (2005).
[34] C. Weeks, J. Hu, J. Alicea, M. Franz, and R. Wu, Phys. Rev. X **1**, 021001 (2011).
[35] A. Möller, U. Low, T. Taetz, M. Kriener, G. Andre, F. Damay, O. Heyer, M. Braden, and J. A. Mydosh, Phys. Rev. B **78**, 024420 (2008).
[36] Y. J. Yan, Z. Y. Li, T. Zhang, X. G. Luo, G. J. Ye, Z. J. Xiang, P. Cheng, L. J. Zou, and X. H. Chen, Phys. Rev. B **85**, 085102 (2012).
[37] D.-Y. Liu, Y. Guo, X.-L. Zhang, J.-L. Wang, Z. Zeng, H.-Q. Lin, and L.-J. Zou, Europhys. Lett. **103**, 47010 (2013).
[38] A. A. Tsirlin, O. Janson, and H. Rosner, Phys. Rev. B **82**, 144416 (2010).
[39] N. F. Q. Yuan, K. F. Mak, and K. T. Law, Phys. Rev. Lett. **113**, 097001 (2014).
[40] J. T. Ye, Y. J. Zhang, R. Akashi, M. S. Bahramy, R. Arita, and Y. Iwasa, Science **338**, 1193 (2012).
[41] J. Vučičevič, M. O. Goerbig, and M. V. Milovanovič, Phys. Rev. B **86**, 214505 (2012).
[42] F. D. M. Haldane, Phys. Rev. Lett. **61**, 2015 (1988).
[43] S. Rachel and K. Le Hur, Phys. Rev. B **82**, 075106 (2010).
[44] J. E. Moore, Nature (London) **464**, 194 (2010).